Journal of the European Ceramic Society 43 (2023) 6982–6988

Contents lists available at ScienceDirect

Journal of the European Ceramic Society

journal homepage: www.elsevier.com/locate/jeurceramsoc

Formation of monolithic $SrTiO_3$-TiO_2 ceramic heterostructures by reactive hydrothermal sintering

Levent Karacasulu [a], Ugur Kartal [a], Oyku Icin [a], Mauro Bortolotti [b], Mattia Biesuz [b], Cekdar Vakifahmetoglu [a,*]

[a] Department of Materials Science and Engineering, Izmir Institute of Technology, 35430 Izmir, Turkey
[b] Department of Industrial Engineering, University of Trento, Via Sommarive 9, 38123 Trento, Italy

ARTICLE INFO

Keywords:
$SrTiO_3$
RHLPD
Cold sintering
Photocatalysis
Electroceramic

ABSTRACT

In a one-pot approach, monolithic $SrTiO_3$-TiO_2 ceramic heterostructures were obtained using the reactive hydrothermal liquid phase densification (rHLPD). Structural, morphological, and photocatalytic properties of the obtained ceramics were analyzed. The relative density of the formed components reached about 80% with reaction time, temperature, and NaOH concentration variation. It was observed via Rietveld refinement that there was no XRD detectable phase other than TiO_2 and $SrTiO_3$ in the final structure. The monolithic $SrTiO_3$-TiO_2 ceramics obtained by hydrothermal reaction at 120 °C for 24 h in 1 M NaOH concentration showed a dielectric constant being around 500, and the dielectric loss was below 0.25 at frequencies higher than 10 kHz. The $SrTiO_3$-TiO_2 heterostructured monoliths having only 20 vol% total porosity and low specific surface area, demonstrated ~60% efficiency (in 5 h) in degrading Methylene Blue photo-catalytically.

1. Introduction

Due to their unique properties, metal oxide perovskites with the chemical formula ABO_3 are commonly used in many areas as solar cells, supercapacitors, light-emitting diodes, and photocatalytic applications [1–5]. Strontium titanate ($SrTiO_3$), one of the perovskite-structured inorganic solids, is a paraelectric material and has been widely used in various applications [6–8]. To obtain a dense component, commercially available $SrTiO_3$ powder is usually pelletized, followed by densification at high temperatures, e.g., between 1250 and 1500 °C, via conventional solid-state sintering [9]. However, this is a time and energy-consuming process [10].

The formation of heterostructures between $SrTiO_3$ and other photocatalytic oxides improves the system's photocatalytic properties [11]. For instance, TiO_2 is characterized by a relatively large band gap (3.2 ev) [12] and suffers the formation of bounded electron-hole pairs, which hinder photocatalytic activity [13]. The combination of titania with $SrTiO_3$, possessing a conduction band edge 200 mV below that of titania, dramatically improves the photocatalytic activity (improved transfer of electron-hole pair) of the system [14,15]. The formation of monolithic $SrTiO_3$-TiO_2 ceramic heterostructures has been investigated only on the particulates processed through complicated strategies [16].

Recent works on sintering inorganic solids have aimed to minimize energy consumption and reduce carbon footprint [17–21]. Among the techniques, the cold sintering process (CSP) and hydrothermal liquid phase densification (rHLPD) are the most promising. Here, the ceramic consolidation is aided at low temperatures by external pressure application and by the addition of a liquid solvent, usually a water solution. The processes have been applied to different ceramics and also to perovskite-structured oxides [22–27], including $SrTiO_3$ [28,29]. While most of the works aimed at maximizing the density of the sintered body (though not always full density could be achieved), the photocatalytic activity is enhanced in porous systems where "sintering" is simply needed to consolidate the body in a solid network. Such results can be easily achieved by the mentioned low-temperature consolidation approaches.

In this context, reactive hydrothermal liquid phase densification (rHLPD) allows the production of ceramic components in one step by combining the synthesis and sintering at low temperatures, eventually yielding direct manufacturing of heterostructured structures [17,23,30]. While many chemical systems were proposed [31], no study focused on the formation, characterization, and application trials of $SrTiO_3$-TiO_2 ceramic heterostructures produced in one step via rHLPD.

---

* Corresponding author.
E-mail addresses: cekdarvakifahmetoglu@iyte.edu.tr, cvahmetoglu@gmail.com (C. Vakifahmetoglu).

https://doi.org/10.1016/j.jeurceramsoc.2023.07.012
Received 28 March 2023; Received in revised form 19 June 2023; Accepted 7 July 2023

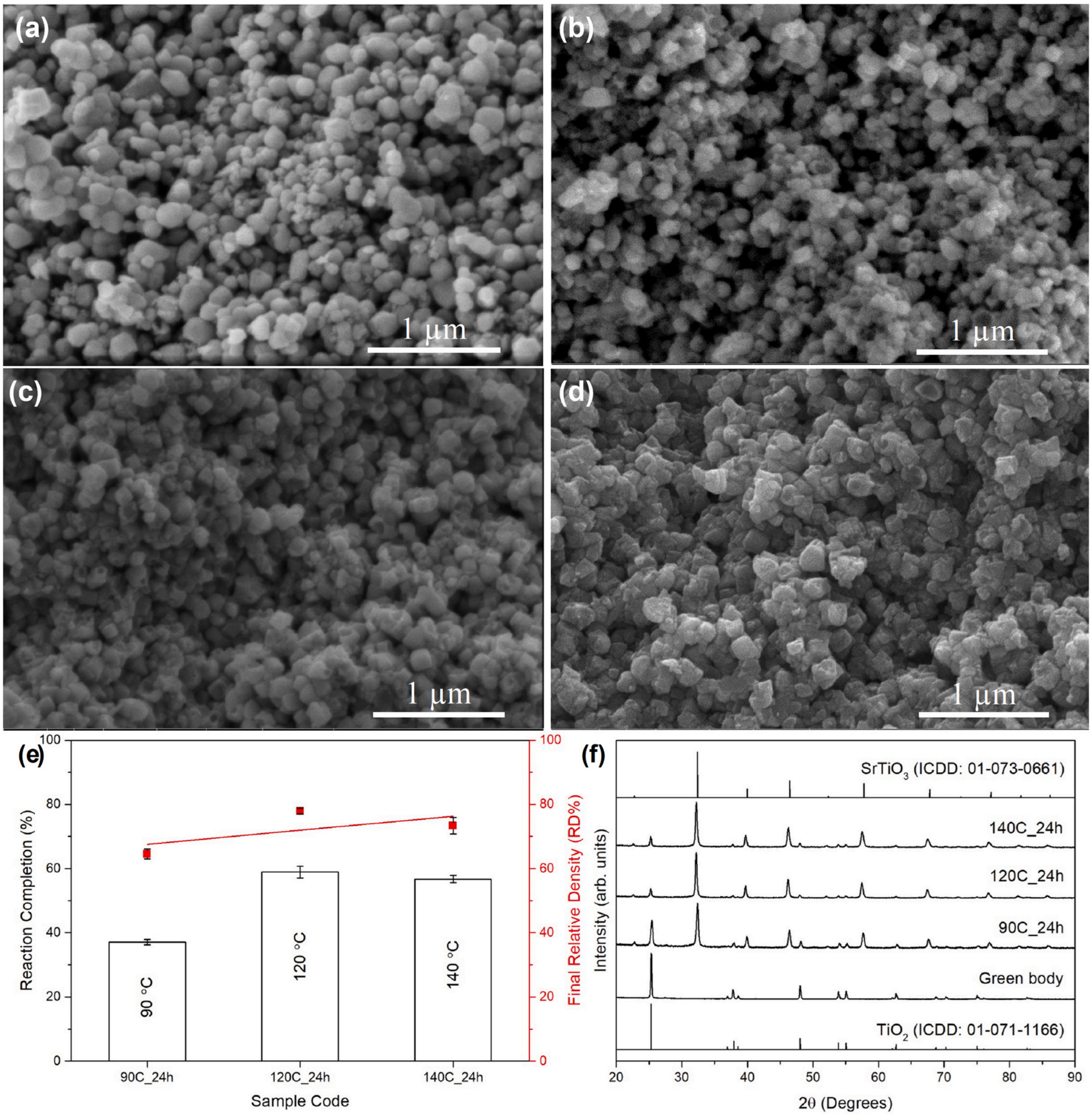

Fig. 1. SEM images obtained from the fractured surfaces of (a) TiO_2 green body, (b-d) pellets obtained from the reactions at different temperatures in 24 h: (b) 90C_24h, (c) 120C_24h, (d) 140C_24h, (e) Reaction completion (%) vs. final relative density (RD%) data of all pellets produced at different temperatures in 24 h, (f) Normalized XRD patterns of TiO_2 green body and rHLPD sintered bodies at different reaction temperatures for 24 h, ICDD #01–071–1166 (TiO_2) and #01–073–0661 ($SrTiO_3$) were also included in the plot.

2. Experimental procedure

All experiments were performed using Strontium hydroxide octahydrate ($Sr(OH)_2.8H_2O$, 99% purity, Alfa Aesar), Titanium dioxide (TiO_2, 99.8% anatase, Merck), Sodium hydroxide (NaOH, 98–100%, Merck), Polyvinyl alcohol (PVA, M_w=31000–50000, 87–89%, Merck) and deionized (DI) water. During the production of $SrTiO_3$ by rHLPD, three different parameters were altered, temperature: 90 C, 120 C, 140 C (°C), time: 6 h, 24 h, 72 h, and NaOH concentration: 0 M (i.e., no NaOH) or 1 M.

To obtain a porous titania matrix, 10 wt% PVA solution and TiO_2 powder were ground in a ball mill (Retsch PM-100, Germany) with yttria-stabilized zirconia (YSZ) balls at 250 rpm for 24 h. After drying, the resulting powder was ground and sieved in a 45-mesh sieve. 0.2 g of sieved powder was pressed in a manual hydraulic press (GS25011, Specac, UK) at 40 MPa. The pellets were treated at 400 °C for 5 h to remove the PVA binder. Then, a 0.3 M $Sr(OH)_2.8H_2O$ solution was prepared and loaded into an autoclave (Parr Instruments 4748 model, USA) for hydrothermal reaction with TiO_2 pellets at 70 vol% filling. After the reaction, the final pellets were washed with DI water and dried at 80 °C overnight.

The fracture surface morphology and elemental composition of the monolithic samples were analyzed by Scanning Electron Microscopy (SEM, FEI, Quanta 250, USA) equipped with Energy Dispersive X-Ray Analysis (EDX) detector. Before SEM analysis, the surfaces of the pellets to be examined were coated with approximately 10 nm Au. In addition, non-coated samples were used for EDS analysis.

X-ray diffraction (XRD) measurements were performed with the Philips X′Pert Pro (Almelo, The Netherlands) device, which is equipped with a Copper anode X-ray source ($Cu_{K\alpha}$ = 1.5406 Å at 40 kV, 30 mA). Rietveld analysis was performed by ReX software [32], starting from the model containing the $SrTiO_3$ and TiO_2 reference crystal structures and refining phases weight fractions as well as their lattice and microstructural parameters. Nitrogen (N_2) gas sorption analyses were done by Gemini V (Micromeritics, Norcross, GA, USA). The samples were degassed at 150 °C for 12 h before examinations. Specific surface area (SSA) was determined from a BET (Brunauer–Emmett– Teller) analysis. The bulk densities of the samples were measured using Archimedes'

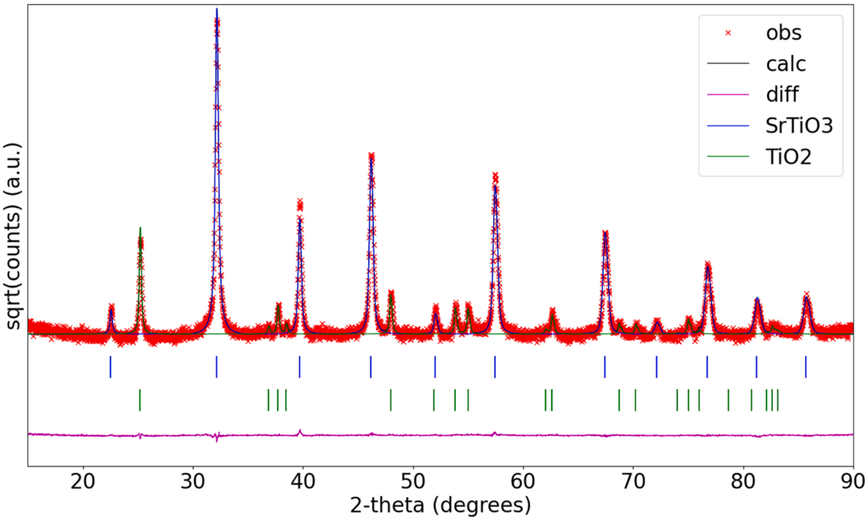

Fig. 2. Rietveld refinement of the x-ray diffraction pattern collected on the sample reacted for 24 h at 120 °C (120C_24h). The red dots correspond to the observed (obs) experimental data, whereas the continuous blue and green profiles represent the modeled signals for the $SrTiO_3$ and TiO_2 phases, respectively. Below the calculated (calc) fit, Bragg reflection positions are marked with the corresponding color code; the residual error (difference: diff) plot is reported in violet.

principle with ethanol. Reaction completion (%) was calculated in two ways. The first one was based on Rietveld phase fractions from XRD data. Secondly, reaction completion values were estimated from the weight change before and after the reaction via Eq. (I) where $Sr(OH)_2$ is the infiltrating species, TiO_2 is the porous solid matrix (green body), and $SrTiO_{3(s)}$ and $H_2O_{(l)}$ are the reaction products.

$$TiO_{2(s)} + Sr(OH)_2 = SrTiO_{3(s)} + H_2O_{(l)} \tag{I}$$

The dielectric constant measurements were obtained using an E4980AL Precision LCR meter (Keysight Technologies, Santa Clara, CA, USA) at room temperature in the 0.02–100 kHz range. As reported previously, the photocatalytic activity was analyzed through time-dependent photodegradation studies of a 2.5 ppm aqueous dye (Methylene Blue, MB) solution [33]. The optical properties were investigated by an ultraviolet-visible (UV–Vis) absorption double beam spectrophotometer (Cary100 Bio; Agilent Technologies Pty Ltd., Mulgrave, VIC, Australia) in a 200–500 nm wavelength range.

3. Results and discussion

The porous green titania body, formed homogeneously over the entire surface, can be seen in the SEM image in Fig. 1(a). As given in Fig. 1(b), the sample reacted at 90 °C also had a porous structure. Instead, when Fig. 1(c) and (d) are analyzed, it can be seen that the microstructures of the samples became denser when the reaction was conducted at 120 °C and 140 °C, respectively.

It is already shown that a porous component can be densified via rHLPD technique without noticeable shrinkage [34]. This is because the crystalline phase of the parent porous substrate changes to another phase having a larger molar volume, i.e., volume expansion contributes to pore closure and densification. Here, in a particular example, titania has a density of (ρ_{TiO_2}) 3.9 g/cm^3, and molar volume of ($V^m_{TiO_2}$) 20.5 cm^3. Instead, $SrTiO_3$ has a density (ρ_{SrTiO_3}) of 5.1 g/cm^3, and molar volume of ($V^m_{SrTiO_3}$) 36 cm^3. If one mole of titania is converted fully to one mole $SrTiO_3$, i.e., 100% reaction yield, a molar volume expansion of ~76% should be expected [35]. Accordingly, when the reaction proceeds via Eq. (I), it yields $SrTiO_3$, a higher molar volumed compound that will cause densification due to pore closure without measurable shrinkage.

The relative densities of TiO_2 green bodies used in all studies were around 52%, i.e., 48 vol% total porosity, taking the theoretical density of 3.9 g/cm^3 (anatase) [36]. The reaction completions (% mole conversion of TiO_2 to $SrTiO_3$) can be assessed from the weight changes for the samples treated at different temperatures, then the estimated values can be used to compute corresponding volume expansions to derive final relative densities (ρ_{bulk} / $\rho_{true_{via\ ROM}}$) after the reaction. As seen in Fig. 1**(e)**, the lowest relative density was observed from the 90 °C reaction, while the highest was found as 78% for the sample reacted at 120 °C for 24 h.

Hydrothermal reactions occurred sparsely in the samples produced at 90 °C, probably due to the limited solubilities of the species. The solubility enhancement determines an increase in the mass transport rates, facilitating the crystallization of $SrTiO_3$ and densification [34,36,37]. The increase in the reaction temperature caused more pronounced densification up to 120 °C. While further experiments are needed to clarify such a point, the slight difference observed for 140 °C treated samples can be due to the differences in the green body relative densities, experimental errors, or aggregated particles observed previously for the synthesis of $SrTiO_3$. Shen et al. [38] demonstrated that as the $SrTiO_3$ hydrothermal reaction temperature increased beyond 120 °C, the $SrTiO_3$ particle size increased irregularly and formed heterogeneous microstructures.

The XRD data of the green pellet was consistent with the anatase phase (ICDD # 01–071–1166), as shown in Fig. 1(f). The characteristic peaks of the $SrTiO_3$ samples appeared at 32.0, 40.0, 46.5, 57.5, 68.0, and 77.0° and can be ascribed to the (110), (111), (200), (211), (220), and (310) planes for the cubic symmetry of $SrTiO_3$, matching well with ICDD # 01–073–0661. Apart from these crystalline phases, the XRD detected no other peaks. While it was not observed, it should be noted that $SrCO_3$ can frequently form as a byproduct when carbon dioxide or carbonate ions are present in the reaction vessel [34,36,37].

Rietveld refinement was conducted on all 24 h treated samples, and a refined pattern of 120C_24h is reported in Fig. 2. For all analyzed samples, nearly full matches with relatively small residual fitting errors can be seen below the example fit. Apart from the marked $SrTiO_3$ and TiO_2 phases, no extra peak was observed for any other crystalline phase (e.g., $SrCO_3$). According to fittings conducted on selected samples, it was found that the 90C_24h had 33 mol%, 120C_24h had 61 mol%, and 140C_24h was found to have reaction completion of 58 mol%. R_{wp} fitness values between 7% and 9% suggest a quite well agreement between the calculated model and the experimental data. The reaction completion calculations were followed in two ways; (i) using the initial and final weights and (ii) the relative phase fractions obtained from the Rietveld analysis, and all the data were compatible. For example, the calculated reaction completion for the 120C_24h sample was around 57 mol% (from weight gain), close to the Rietveld fitting result of

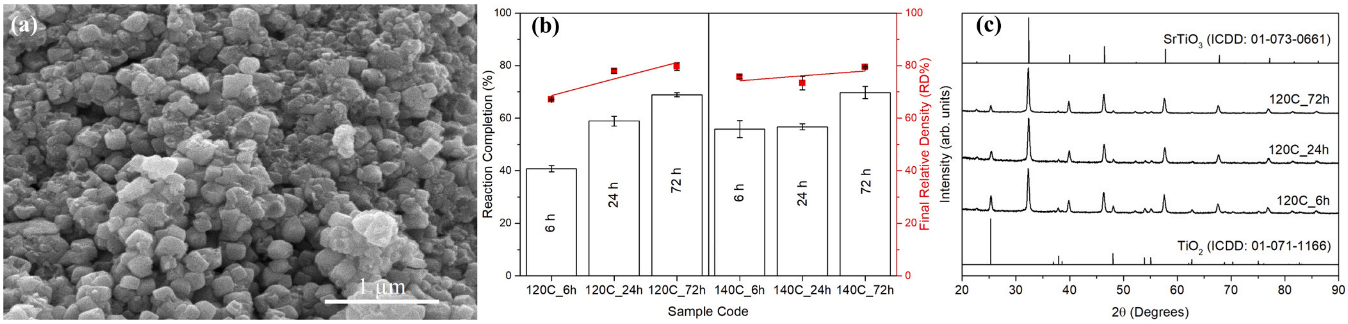

Fig. 3. (a) SEM micrograph taken from the fractured surface of 120C_72h sample, **(b)** Reaction completion (%) vs. final relative density (RD%) graph of all pellets produced at different temperatures in 24 h at 120 °C and 140 °C, **(c)** XRD pattern of samples obtained at 120 °C in different reaction times (6, 24, and 72 h).

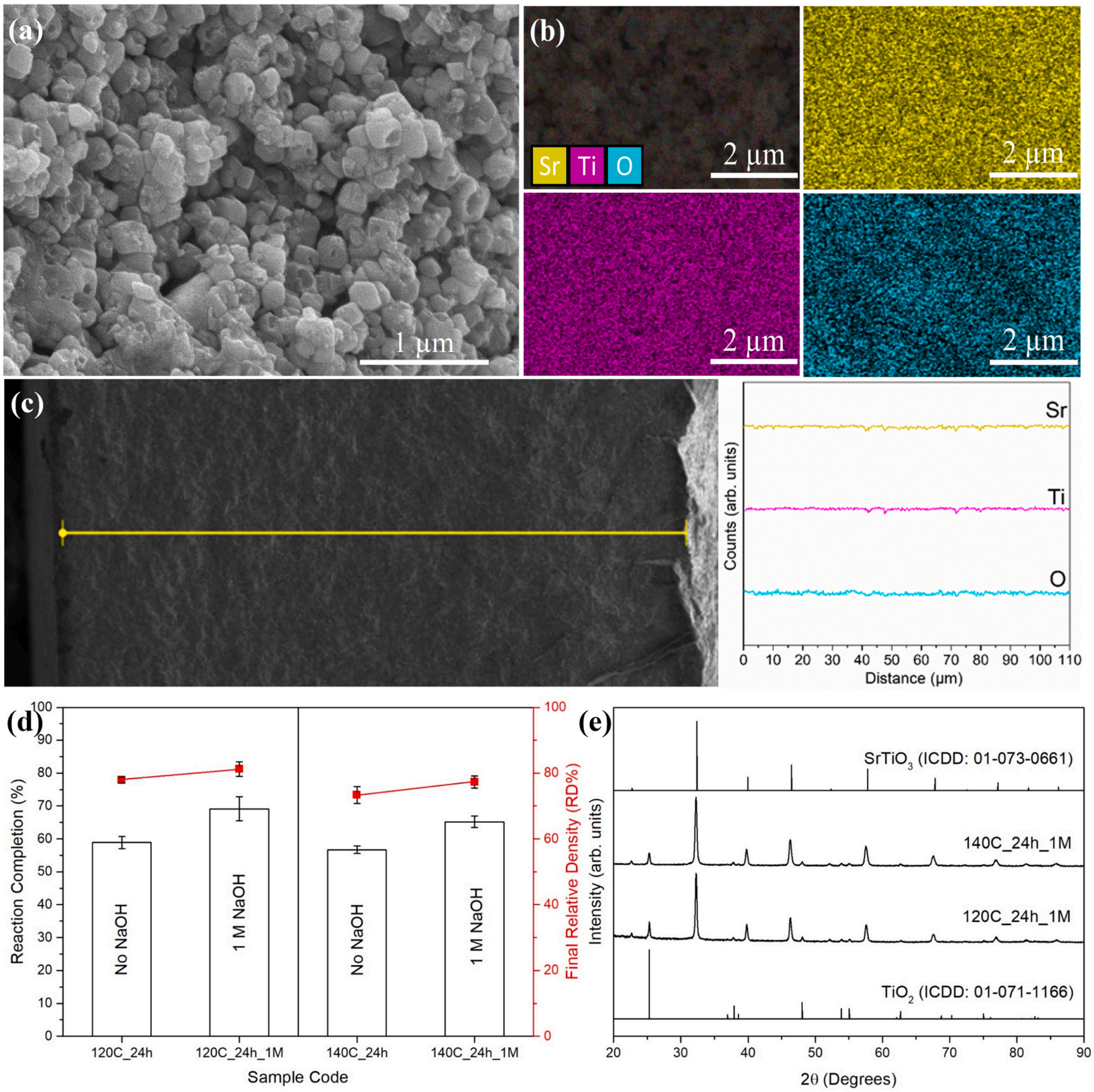

Fig. 4. (a) SEM images of the fractured surface of the 120C_24h_1M pellet obtained at 120 °C in 24 h under 1 M NaOH concentration condition, (b) EDX mapping from the center of the fracture surface of the 120C_24h_1M pellet, (c) EDX scan from the top surface to 110 µm depth, (d) Reaction completion (%) vs. final relative density (RD%) graph of all pellets produced at 120 °C and 140 °C in different NaOH concentrations (without NaOH and 1 M). (e) XRD pattern of samples obtained at 120 °C and 140 °C in 1 M NaOH concentration.

61 mol%. As a result, if one calculates the volume expansion related to such a mole conversion through reaction (I), a final relative density of 77%, similar to the one obtained from Archimedes' measurement of 78% can be observed.

SEM micrograph taken from the fractured surface of the sample reacted for 72 h at 120 °C (120C_72h) is shown in Fig. 3(a). At different temperatures, relatively dense microstructures were obtained for longer reaction times, affecting the nucleation rate [39]. The relative density

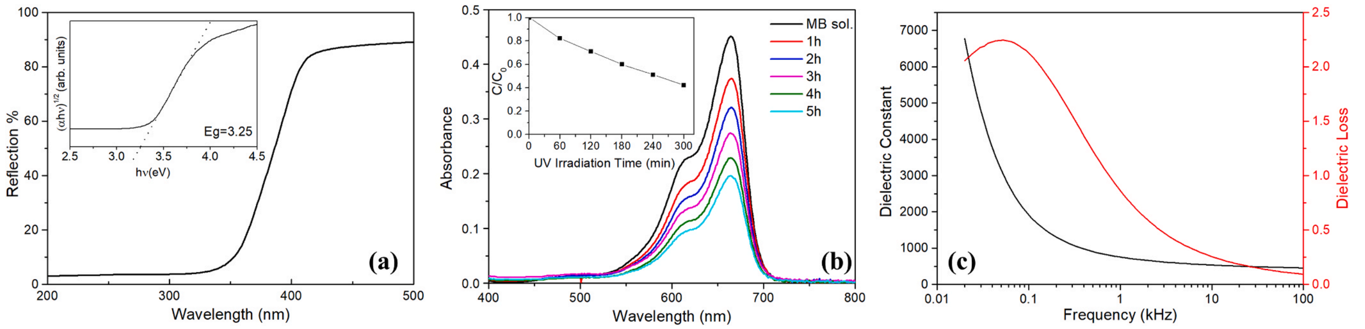

Fig. 5. (a) Reflectance spectra of 120C_24h_1M (obtained at 120 °C in 24 h under 1 M NaOH concentration) pellet (the top-left inset represents Kubelka–Munk plot of reflectance spectra to calculate the band gap energy), (b) UV-Vis absorption spectra showing the photocatalytic degradation of Methylene Blue dye using 120C_24h_1M pellet under UV-Vis irradiation (the top-left inset represents concentration change of Methylene Blue vs. UV-Vis irradiation time), and **(c)** Frequency-dependent dielectric constant and dielectric loss of the same sample obtained at room temperature.

change with different reaction times is demonstrated in Fig. 3(b). When the reaction was conducted for 72 h, comparable relative density values of around 80% were observed.

While the increase in reaction time caused enhanced $SrTiO_3$ formation, it is essential to note that the kinetics was slower than those for the other rHLPD studies [23,30]. Similar observations were reported for hydrothermal synthesis of $SrTiO_3$ using anatase to react at 200 °C. A significant amount of unreacted titania was found even after 48 h of reaction [36,40–42]. XRD data obtained from the samples reacted for different periods at 120 °C (see Fig. 3(c)) and 140 °C (data not shown for brevity) demonstrates merely the formation of a $SrTiO_3$-TiO_2 ceramic heterostructure system.

SEM image taken from the fracture surface of the 120C_24h_1M sample, obtained from the reaction at 120 °C for 24 h, under 1 M NaOH concentration, is given in Fig. 4(a). A homogeneous microstructure can be seen, as in all other samples. When the EDX images obtained from the fracture surface (Fig. 4(b)) are analyzed, it is possible to see that Sr, Ti, and O are homogeneously distributed, but no Na was observed over the entire scanned pellet surface. The examination was also conducted from the top surface to 110 μm depth (see Fig. 4(c)), and consistently, only Sr, Ti, and O were found. Accordingly, it is possible to state that the reaction proceeded virtually homogenous throughout the sample. Since the formation of $SrTiO_3$ necessitates the parent titania surface, the structure was probably composed of anatase-TiO_2-cored $SrTiO_3$, as documented in previous hydrothermal reaction studies [36].

The final relative density of the pellets obtained by rHLPD experiments performed at 1 M NaOH concentration is shown in Fig. 4(d). Similar to other studies, the tendency of $SrTiO_3$ formation increased with NaOH, i.e., NaOH enhanced the sample relative densities and reaction conversions [43]. It was already documented that the $SrTiO_3$ synthesis is supported by increased alkalinity [34,43]. Lencka and Riman constructed a Sr-Ti-H_2O stability diagram based on theoretical calculations. The authors showed that the $SrTiO_3$ formation from TiO_2 requires an alkaline medium for enhanced dissolution of TiO_2 and subsequent precipitation of $SrTiO_3$ [34,37,44].

The XRD analysis of the samples reacted under 1 M NaOH concentrations is given in Fig. 4(e). When the XRD patterns are examined, clear peaks of $SrTiO_3$ and TiO_2 without additional crystalline phases can be seen in all samples, corroborating that $SrTiO_3$ is the predominant reaction product in the experimental conditions [36].

An indirect optical band gap (E_g) value of 3.25 eV, similarly observed for $SrTiO_3$-TiO_2 heterostructures [15], was found using Kubelka-Munk transformation (see Fig. 5(a-inset)) from reflectance spectra (shown in Fig. 5(a)). Fig. 5(b) demonstrates the photocatalytic performance of the 120C_24h_1M pellet with only 20 vol% total porosity. The intensity of absorption peaks decreased with time, and the degradation efficiency of MB dye was around 60% in 5 h. The change in the concentration of MB vs. UV-Vis irradiation time can be seen in Fig. 5(b-inset). Although the 120C_24h_1M sample had a low SSA of 5.7 m^2/g, it showed better degradation efficiency with a higher photodegradation rate constant (0.0028 min^{-1}) than other monolithic $SrTiO_3$-TiO_2 and N-doped $SrTiO_3$-TiO_2 systems with approximately five times larger surface area of 27.8 m^2/g [45,46].

The dielectric constant and dielectric loss curves obtained from the same sample (120C_24h_1M) are shown in Fig. 5(c). The dielectric constant was around 500 at high frequencies (above 10 kHz), and the dielectric loss decreased significantly above 10 kHz, falling below 0.25 [47]. A few recent works proposed ferroelectricity-based photocatalysts with enhanced photocatalytic performance due probably to the polarization-dependent band bending of $BaTiO_3$ [48]. While $SrTiO_3$ is paraelectric and the correlation of dielectric properties with the photocatalytic performance of TiO_2-$SrTiO_3$ heterostructured monoliths is beyond the scope of the present work, further investigations are of interest.

4. Conclusions

$SrTiO_3$-TiO_2 monolithic ceramic heterostructures were produced using a novel cold sintering technique called rHLPD· The effect of different temperatures, time, and NaOH concentrations was investigated. Only $SrTiO_3$ and TiO_2 were observed within the limits of the XRD technique, i.e., no extra peaks resolvable for any other crystalline phase were observed. The optimum reaction parameters were set at 120 °C for 24 h with 1 M NaOH, yielding ~80% dense components having reaction completion of 69 mol%. The dielectric constant measurements demonstrated that at high frequencies above 10 kHz, the dielectric constant was around 500, and the dielectric loss value was below 0.25. The monolithic $SrTiO_3$-TiO_2 ceramic pellets with 20 vol% total porosity were used to degrade Methylene Blue dye photo-catalytically, and ~60% efficiency was observed in 5 h.

Funding

This research received no specific grant from funding agencies in the public, commercial, or not-for-profit sectors.

Declaration of Competing Interest

The authors declare that they have no known competing financial interests or personal relationships that could have appeared to influence the work reported in this paper.

Acknowledgments

The authors thank Dr. Merve Gunnar Karakaya and Assoc. Prof. Dr. Umut Adem from the Izmir Institute of Technology (IZTECH, Izmir, Turkey) for the electrical analysis, and Yusuf Tutel from the Nanolab at the Middle East Technical University (METU, Ankara, Turkey) for UV-Vis spectroscopy analysis. We thank Esin Karatas for the initial work during her M.Sc. studies supervised by Cekdar Vakif Ahmetoglu (Ph.D.) at the Izmir Institute of Technology. We acknowledge Ege Yılmaz for his help preparing plots and the IZTECH Center for Materials Research for XRD and SEM investigations.

References

[1] P. Liu, N. Han, W. Wang, R. Ran, W. Zhou, Z. Shao, High-quality ruddlesden–popper perovskite film formation for high-performance perovskite solar cells, Adv. Mater. 33 (2021), 2002582, https://doi.org/10.1002/adma.202002582.

[2] H.-Y. Kim, J. Shin, I.-C. Jang, Y.-W. Ju, Hydrothermal synthesis of three-dimensional perovskite $NiMnO_3$ oxide and application in supercapacitor electrode, Energy 13 (2019) 36, https://doi.org/10.3390/en13010036.

[3] A. Fakharuddin, M.K. Gangishetty, M. Abdi-Jalebi, S.-H. Chin, AbdR. bin Mohd Yusoff, D.N. Congreve, W. Tress, F. Deschler, M. Vasilopoulou, H.J. Bolink, Perovskite light-emitting diodes, Nat. Electron. 5 (2022) 203–216, https://doi.org/10.1038/s41928-022-00745-7.

[4] S. Tasleem, M. Tahir, Recent progress in structural development and band engineering of perovskites materials for photocatalytic solar hydrogen production: a review, Int. J. Hydrog. Energy 45 (2020) 19078–19111, https://doi.org/10.1016/j.ijhydene.2020.05.090.

[5] K. Wei, Y. Faraj, G. Yao, R. Xie, B. Lai, Strategies for improving perovskite photocatalysts reactivity for organic pollutants degradation: a review on recent progress, Chem. Eng. J. 414 (2021), 128783, https://doi.org/10.1016/j.cej.2021.128783.

[6] J. Sun, T. Gao, X. Song, Y. Zhao, Y. Lin, H. Wang, D. Ma, Y. Chen, W. Xiang, J. Wang, Y. Zhang, Z. Liu, Direct growth of high-quality graphene on high-κ dielectric $SrTiO_3$ substrates, J. Am. Chem. Soc. 136 (2014) 6574–6577, https://doi.org/10.1021/ja5022602.

[7] H. Zhan, Z.-G. Chen, J. Zhuang, X. Yang, Q. Wu, X. Jiang, C. Liang, M. Wu, J. Zou, Correlation between multiple growth stages and photocatalysis of $SrTiO_3$ nanocrystals, J. Phys. Chem. C. 119 (2015) 3530–3537, https://doi.org/10.1021/jp512448p.

[8] S.A. Hayward, E.K.H. Salje, Cubic-tetragonal phase transition in $SrTiO_3$ revisited: Landau theory and transition mechanism, Phaes Transit. 68 (1999) 501–522, https://doi.org/10.1080/01411599908224530.

[9] M. Bäurer, H. Kungl, M.J. Hoffmann, Influence of Sr/Ti stoichiometry on the densification behavior of strontium titanate, J. Am. Ceram. Soc. 92 (2009) 601–606, https://doi.org/10.1111/j.1551-2916.2008.02920.x.

[10] W. Bian, X. Lu, Y. Li, C. Min, H. Zhu, Z. Fu, Q. Zhang, Influence of Nd doping on microwave dielectric properties of $SrTiO_3$ ceramics, J. Mater. Sci. Mater. Electron 29 (2018) 2743–2747, https://doi.org/10.1007/s10854-017-8201-y.

[11] Y. Zhao, Y. Guo, J. Li, P. Li, Efficient hydrogen evolution with ZnO/$SrTiO_3$ S-scheme heterojunction photocatalyst sensitized by Eosin Y, Int. J. Hydrog. Energy 46 (2021) 18922–18935, https://doi.org/10.1016/j.ijhydene.2021.03.051.

[12] R.V. Nair, V.S. Gummaluri, M.V. Matham, V. C, A review on optical bandgap engineering in TiO_2 nanostructures via doping and intrinsic vacancy modulation towards visible light applications, J. Phys. D. Appl. Phys. 55 (2022), 313003, https://doi.org/10.1088/1361-6463/ac6135. V.C.

[13] X. Wang, R.A. Caruso, Enhancing photocatalytic activity of titania materials by using porous structures and the addition of gold nanoparticles, J. Mater. Chem. 21 (2011) 20–28, https://doi.org/10.1039/C0JM02620D.

[14] T. Cao, Y. Li, C. Wang, C. Shao, Y. Liu, A facile in situ hydrothermal method to $SrTiO_3$/TiO_2 nanofiber heterostructures with high photocatalytic activity, Langmuir 27 (2011) 2946–2952, https://doi.org/10.1021/la104195v.

[15] J. Zhang, J.H. Bang, C. Tang, P.V. Kamat, Tailored $TiO_2-SrTiO_3$ heterostructure nanotube arrays for improved photoelectrochemical performance, ACS Nano 4 (2010) 387–395, https://doi.org/10.1021/nn901087c.

[16] E.-C. Su, B.-S. Huang, J.-T. Lee, M.-Y. Wey, Excellent dispersion and charge separation of $SrTiO_3$-TiO_2 nanotube derived from a two-step hydrothermal process for facilitating hydrogen evolution under sunlight irradiation, Sol. Energy 159 (2018) 751–759, https://doi.org/10.1016/j.solener.2017.11.048.

[17] C. Vakifahmetoglu, L. Karacasulu, Cold sintering of ceramics and glasses: a review, Curr. Opin. Solid State Mater. Sci. 24 (2020), 100807, https://doi.org/10.1016/j.cossms.2020.100807.

[18] M. Biesuz, S. Grasso, V.M. Sglavo, What's new in ceramics sintering? A short report on the latest trends and future prospects, Curr. Opin. Solid State Mater. Sci. 24 (2020), 100868, https://doi.org/10.1016/j.cossms.2020.100868.

[19] A. Galotta, V.M. Sglavo, The cold sintering process: a review on processing features, densification mechanisms and perspectives, J. Eur. Ceram. Soc. 41 (2021) 1–17, https://doi.org/10.1016/j.jeurceramsoc.2021.09.024.

[20] J. Guo, R. Floyd, S. Lowum, J.-P. Maria, T. Herisson de Beauvoir, J.-H. Seo, C. A. Randall, Cold sintering: progress, challenges, and future opportunities, Annu. Rev. Mater. Res. 49 (2019) 275–295, https://doi.org/10.1146/annurev-matsci-070218-010041.

[21] H. Guo, A. Baker, J. Guo, C.A. Randall, Cold sintering process: a novel technique for low-temperature ceramic processing of ferroelectrics, J. Am. Ceram. Soc. 99 (2016) 3489–3507, https://doi.org/10.1111/jace.14554.

[22] H. Guo, J. Guo, A. Baker, C.A. Randall, Hydrothermal-assisted cold sintering process: a new guidance for low-temperature ceramic sintering, ACS Appl. Mater. Interfaces 8 (2016) 20909–20915, https://doi.org/10.1021/acsami.6b07481.

[23] L. Karacasulu, M. Tokkan, M. Bortolotti, G. Ischia, U. Adem, C. Vakifahmetoglu, Electrical characteristics of low temperature densified barium titanate, Ceram. Int. 46 (2020) 16670–16676, https://doi.org/10.1016/j.ceramint.2020.03.240.

[24] J.-P. Ma, X.-M. Chen, W.-Q. Ouyang, J. Wang, H. Li, J.-L. Fang, Microstructure, dielectric, and energy storage properties of $BaTiO_3$ ceramics prepared via cold sintering, Ceram. Int. 44 (2018) 4436–4441, https://doi.org/10.1016/j.ceramint.2017.12.044.

[25] H.-Z. Shen, N. Guo, P. Shen, Synthesis and densification of $BaZrO_3$ ceramics by reactive cold sintering of $Ba(OH)_2{\cdot}8H_2O$-$Zr(OH)_4$ powders, J. Eur. Ceram. Soc. 43 (2023) 392–400, https://doi.org/10.1016/j.jeurceramsoc.2022.10.016.

[26] P. Castellani, C. Nicollet, E. Quarez, O. Joubert, A. Le Gal La Salle, Synthesis of yttrium doped barium Zirconate/Cerate electrolyte materials and densification using conventional and cold-sintering processes, ECS Trans. 109 (2022) 13, https://doi.org/10.1149/10913.0013ecst.

[27] V.L. Vilesh, N. Santha, G. Subodh, Influence of Li_2MoO_4 and polytetrafluoroethylene addition on the cold sintering process and dielectric properties of $BaBiLiTeO_6$ ceramics, Ceram. Int. 47 (2021) 30756–30763, https://doi.org/10.1016/j.ceramint.2021.07.255.

[28] R. Boston, J. Guo, S. Funahashi, A.L. Baker, I.M. Reaney, C.A. Randall, Reactive intermediate phase cold sintering in strontium titanate, RSC Adv. 8 (2018) 20372–20378, https://doi.org/10.1039/C8RA03072C.

[29] N. Guo, H.-Z. Shen, P. Shen, One-step synthesis and densification of $BaTiO_3$ by reactive cold sintering, Scr. Mater. 213 (2022), 114628, https://doi.org/10.1016/j.scriptamat.2022.114628.

[30] C. Vakifahmetoglu, J.F. Anger, V. Atakan, S. Quinn, S. Gupta, Q. Li, L. Tang, R. E. Riman, Reactive hydrothermal liquid-phase densification (rHLPD) of ceramics - a study of the BaTiO $_3$ [TiO $_2$] composite system, J. Am. Ceram. Soc. 99 (2016) 3893–3901, https://doi.org/10.1111/jace.14468.

[31] R.E. Riman, V. Atakan, Method of hydrothermal liquid phase sintering of ceramic materials and products derived therefrom, US Patent 8,313,802, (2012).

[32] M. Bortolotti, L. Lutterotti, I. Lonardelli, ReX: a computer program for structural analysis using powder diffraction data, J. Appl. Crystallogr 42 (2009) 538–539, https://doi.org/10.1107/S0021889809008309.

[33] O. Icin, C. Vakifahmetoglu, Dye removal by polymer derived ceramic nanobeads, Ceram. Int. 47 (2021) 27050–27057, https://doi.org/10.1016/j.ceramint.2021.06.118.

[34] M.M. Lencka, R.E. Riman, Hydrothermal synthesis of perovskite materials: thermodynamic modeling and experimental verification, Ferroelectrics 151 (1994) 159–164, https://doi.org/10.1080/00150199408244737.

[35] A. Saboori, X. Chen, C. Badini, P. Fino, M. Pavese, Reactive spontaneous infiltration of Al-activated TiO2 by molten aluminum, Trans. Nonferrous Met. Soc. China 29 (2019) 657–666, https://doi.org/10.1016/S1003-6326(19)64976-9.

[36] V. Kalyani, B.S. Vasile, A. Ianculescu, A. Testino, A. Carino, M.T. Buscaglia, V. Buscaglia, P. Nanni, Hydrothermal synthesis of $SrTiO_3$: role of interfaces, Cryst. Growth Des. 15 (2015) 5712–5725, https://doi.org/10.1021/acs.cgd.5b00770.

[37] G. Canu, V. Buscaglia, Hydrothermal synthesis of strontium titanate: thermodynamic considerations, morphology control and crystallisation mechanisms, CrystEngComm 19 (2017) 3867–3891, https://doi.org/10.1039/C7CE00834A.

[38] H. Shen, Y. Lu, Y. Wang, Z. Pan, G. Cao, X. Yan, G. Fang, Low temperature hydrothermal synthesis of $SrTiO_3$ nanoparticles without alkali and their effective photocatalytic activity, J. Adv. Ceram. 5 (2016) 298–307, https://doi.org/10.1007/s40145-016-0203-3.

[39] Y. Zhang, L. Zhong, D. Duan, A single-step direct hydrothermal synthesis of SrTiO3 nanoparticles from crystalline P25 TiO_2 powders, J. Mater. Sci. 51 (2016) 1142–1152, https://doi.org/10.1007/s10853-015-9445-7.

[40] V. Kalyani, B.S. Vasile, A. Ianculescu, M.T. Buscaglia, V. Buscaglia, P. Nanni, Hydrothermal synthesis of $SrTiO_3$ mesocrystals: single crystal to mesocrystal transformation induced by topochemical reactions, Cryst. Growth Des. 12 (2012) 4450–4456, https://doi.org/10.1021/cg300614f.

[41] L. Fang, E. Hu, X. Hu, Z. Jiang, M.A.K.Y. Shah, J. Wang, F. Wang, Development of a core–shell heterojunction TiO_2/$SrTiO_3$ electrolyte with improved ionic conductivity, ChemPhysChem 23 (2022), e202200314, https://doi.org/10.1002/cphc.202200314.

[42] J. Ng, S. Xu, X. Zhang, H.Y. Yang, D.D. Sun, Hybridized nanowires and cubes: a novel architecture of a heterojunctioned TiO_2/$SrTiO_3$ thin film for efficient water splitting, Adv. Funct. Mater. 20 (2010) 4287–4294, https://doi.org/10.1002/adfm.201000931.

[43] S.-T. Huang, W.W. Lee, J.-L. Chang, W.-S. Huang, S.-Y. Chou, C.-C. Chen, Hydrothermal synthesis of $SrTiO_3$ nanocubes: Characterization, photocatalytic activities, and degradation pathway, J. Taiwan Inst. Chem. Eng. 45 (2014) 1927–1936, https://doi.org/10.1016/j.jtice.2014.02.003.

[44] M.M. Lencka, R.E. Riman, Thermodynamics of the hydrothermal synthesis of calcium titanate with reference to other alkaline-earth titanates, Chem. Mater. 7 (1995) 18–25, https://doi.org/10.1021/cm00049a006.

[45] O. Ruzimuradov, S. Nurmanov, M. Hojamberdiev, R.M. Prasad, A. Gurlo, J. Broetz, K. Nakanishi, R. Riedel, Preparation and characterization of macroporous $TiO_2-SrTiO_3$ heterostructured monolithic photocatalyst, Mater. Lett. 116 (2014) 353–355, https://doi.org/10.1016/j.matlet.2013.11.065.

[46] O. Ruzimuradov, K. Sharipov, A. Yarbekov, K. Saidov, M. Hojamberdiev, R. M. Prasad, G. Cherkashinin, R. Riedel, A facile preparation of dual-phase nitrogen-doped $TiO_2-SrTiO_3$ macroporous monolithic photocatalyst for organic dye

photodegradation under visible light, J. Eur. Ceram. Soc. 35 (2015) 1815–1821, https://doi.org/10.1016/j.jeurceramsoc.2014.12.023.

[47] Z. Wang, M. Cao, Z. Yao, Q. Zhang, Z. Song, W. Hu, Q. Xu, H. Hao, H. Liu, Z. Yu, Giant permittivity and low dielectric loss of $SrTiO_3$ ceramics sintered in nitrogen atmosphere, J. Eur. Ceram. Soc. 34 (2014) 1755–1760, https://doi.org/10.1016/j.jeurceramsoc.2014.01.015.

[48] G. Panthi, M. Park, Approaches for enhancing the photocatalytic activities of barium titanate: a review, J. Energy Chem. 73 (2022) 160–188, https://doi.org/10.1016/j.jechem.2022.06.023.